energies

MDPI

Article

Electric Field Distortion and Insulation Response Characteristics of Typical Defects in 35 kV Oil-Impregnated Paper Bushings

Yuandi Lin [1], Tonglei Wang [1], Peng Wu [1], Jun Jiang [2] and Jianning Zhao [2,*]

[1] State Grid JiangSu Electric Power Company, Nanjing 211103, China
[2] Jiangsu Key Laboratory of New Energy Generation and Power Conversion, Nanjing University of Aeronautics and Astronautics, Nanjing 211106, China
* Correspondence: zhaojianning1025@163.com

Abstract

Oil-impregnated paper (OIP) capacitive bushings are critical insulation components of power transformers, and internal defect.0s may induce partial discharge (PD) and further lead to insulation breakdown, threatening equipment safety and power supply reliability. This study investigates the electric field distribution and insulation response characteristics of four typical defects in a 35 kV OIP bushing, including serrated cuts at the edge of the capacitor foil, metallic tips between capacitor screens, internal creepage along the lower porcelain insulator, and poor grounding of the end screen. First, full-scale three-dimensional models of normal and defective bushings are established to analyse the effects of different defects on electric field distribution and dielectric response parameters. Corresponding defective specimens are then fabricated, and dielectric parameter measurements and partial discharge tests are performed to verify the simulation results. The simulation results indicate that the maximum electric field strengths at the defect locations of the serrated foil, metallic tip, and internal creepage defects reach 8.92 kV/mm, 2.82 kV/mm, and 12.19 kV/mm, respectively, while their influences on dielectric response parameters are limited. In contrast, the loss of end-screen grounding increases the end-screen potential to approximately 26 kV and causes significant variations in dielectric parameters. The experimental results are highly consistent with the simulation analysis. This study reveals the electric field distortion mechanisms and response differences associated with typical bushing defects, providing theoretical support for defect mechanism analysis and insulation condition assessment.

Keywords: oil-impregnated paper insulation; capacitive bushing; typical defects; electric field distortion; dielectric response; partial discharge

Check for updates

Academic Editor: Krzysztof Górecki

Received: 25 September 2026
Revised: 23 October 2026
Accepted: 28 October 2026
Published: 30 October 2026

Copyright: © 2026 by the authors. Licensee MDPI, Basel, Switzerland. This article is an open access article distributed under the terms and conditions of the Creative Commons Attribution (CC BY) license.

1. Introduction

Oil-impregnated paper (OIP) condenser bushings are critical components connecting transformer windings to the grid, providing insulation, field grading, and mechanical support. Widely used for decades owing to high dielectric strength and mature processes [1], they are subjected to electrical, thermal, mechanical, and environmental stresses that alter insulation and field distribution [2]. Manufacturing defects, assembly anomalies, and ageing may introduce foil damage, foreign particles, creepage, or end-screen grounding issues [3], causing field concentration, partial discharge (PD), and breakdown, thus threatening reliability [4,5]. Studying defect effects is, therefore, important.

Current condition assessment mainly uses dielectric response and PD. Frequency-domain spectroscopy (FDS) evaluates moisture and ageing via the dissipation factor and

capacitance [6], with improvements like temperature normalisation and high-voltage FDS [7–9]. However, FDS is insensitive to localised defects. PD directly detects field enhancement; phase-resolved partial discharge (PRPD) and ultra-high-frequency (UHF) methods aid discharge identification and location [10,11], while PD behaviour relates to defect morphology and field distribution [12]. External measurements alone cannot fully reveal the defect-structure relation.

Finite element simulation is increasingly applied. Studies show that electrode edges, metallic tips, and discontinuities enhance the field and reduce margins [13,14]. Models of complex capacitive screens analyse design and operating effects [15]. For voids and metal particles, combined simulation and experiments link defect locations to PD [16,17]; local field enhancement is key, governed by defect geometry [18]. However, simulations often use simplified geometries and focus on the maximum field, lacking dielectric parameter changes and experimental correlations.

Different defects exhibit distinct mechanisms: sawtooth and metal tips enhance the field via the tip effect; creepage causes tangential field concentration; and end-screen grounding alters potential distribution. Realistic bushing models are needed. Artificial defects, combined with dielectric and PD tests, have been used [19–21], and model–structure consistency affects simulation reliability [22]. Yet, systematic studies on 35 kV full-scale OIP bushings covering defect–structure–field–dielectric–PD relationships are scarce [23–25].

This paper studies a 35 kV OIP bushing, establishing full-scale 3D models for normal and four defect types: sawtooth, metal tips, creepage, and end-screen loss. It analyses the field, capacitance, and dielectric loss. Defective specimens are fabricated and tested to validate simulations. The aim is to reveal field distortion mechanisms and insulation response differences, providing a basis for defect studies and diagnostic optimisation.

2. Full-Scale Model Simulation of Normal OIP Bushing

2.1. The Basic Structure of the OIP Bushing

The external part of an OIP condenser bushing is a high-strength porcelain, which provides external insulation, mechanical protection, and sealing to protect the internal insulating medium. The core insulating element inside is the condenser core, which is made by alternately winding insulating paper and aluminium foil, followed by vacuum drying and oil impregnation. This structure uniformises the electric field distribution and effectively avoids localised field concentrations in both the radial and axial directions. The conductor rod passing through the centre carries the rated operating current. A flange is provided in the middle of the bushing for fixing to the equipment tank, sealing, and earthing. An oil conservator at the top compensates for volume changes of the insulating oil due to temperature variations, maintains a slight internal positive pressure, and prevents the ingress of moisture and contaminants.

2.2. Parameter Calculation of the OIP Bushing

When insulation degradation occurs inside the bushing, for example, when moisture ingress changes the permittivity or when partial discharge causes breakdown and short-circuiting between adjacent capacitive screens, both the main-screen capacitance C_1 and the end-screen capacitance C_2 change significantly. Therefore, the capacitance parameters of the bushing are directly related to its insulation condition, and accurate determination of these capacitance parameters is a prerequisite for monitoring the bushing health. Since the radial dimension of the bushing is much smaller than the axial dimension, edge effects can be neglected. Based on the fundamental principles of electrostatics, the capacitance C_i of

the i-th layer of the condenser core can be approximated using the concentric cylindrical capacitor formula:

$$C_i = \frac{2\pi\varepsilon_0\varepsilon_r l_i}{\ln(r_{i+1}/r_i)} \tag{1}$$

where ε_0 is the vacuum permittivity, taking the value of 8.854×10^{-12} (F/m); ε_r is the relative permittivity of oil-impregnated paper, dimensionless; l_i is the effective axial length of the i-th capacitive screen, in (m); r_i and r_{i+1} are the inner and outer radii of the i-th insulation layer, in (m); and C_i is the inter-layer capacitance of the i-th insulation layer, in (F).

To achieve an optimised radial electric field distribution, the capacitance of each unit is designed to be equal or to vary according to a predetermined rule, so that the voltage difference across each layer of insulating paper remains essentially uniform, thereby avoiding local field concentration.

The main-screen capacitance (main insulation) is the equivalent capacitance obtained by connecting in series all capacitances from the conductor rod (high-voltage terminal) to the end-screen lead (test terminal). Assuming that the end screen is located at the k-th layer, the main-screen capacitance C_1 is the series equivalent of the first k capacitances:

$$C_1 = \left(\sum_{i=1}^{k} \frac{1}{C_i}\right) \tag{2}$$

The end-screen capacitance is the equivalent capacitance of the insulation layer (usually a single layer or a small number of layers in series) between the end-screen lead and the outermost earthed flange. Typically, the end screen is the penultimate capacitive screen, connected to the outside via a lead, with the central conductor rod as the 0-th electrode plate and the outermost layer (the n-th layer) as the earthed flange. The end-screen capacitance C_2 is, therefore, the series equivalent of the capacitances from the $(k+1)$ -th layer to the n-th layer:

$$C_2 = \left(\sum_{i=k+1}^{n} \frac{1}{C_i}\right)^{-1} \tag{3}$$

In most standard bushing designs, the end screen is located immediately inside the flange, i.e., the end screen is the $(n-1)$ -th layer and the flange is the n-th layer. In this case, there is only one insulation layer for the end screen, and thus:

$$C_2 = C_n = \frac{2\pi\varepsilon_0\varepsilon_r l_n}{\ln(r_{n+1}/r_n)} \tag{4}$$

In addition, the dielectric loss factor (dissipation factor) is the ratio of the active current to the reactive current in the insulating medium under AC voltage and is a key parameter for assessing the health condition of the bushing insulation. For an ideal capacitor, the reactive current is large, the active power loss is extremely low, and the tanδ value is very small. When the insulating material is affected by moisture, ageing, contamination, or the formation of conductive paths, the active power loss increases significantly, leading to a rise in tanδ. Therefore, the dissipation factor is a critical macroscopic indicator for evaluating the insulation state of bushings. In dielectric physics, the loss tangent can be expressed as:

$$\tan\delta = \frac{\varepsilon''}{\varepsilon'} \tag{5}$$

where ε' is the real part of the complex permittivity (relative permittivity) and ε'' is the imaginary part of the complex permittivity (loss factor).

In frequency-domain simulations, if the conductivity σ and the real part of the complex permittivity ε' are used, the equivalent imaginary part of the complex permittivity is related to the conductivity by:

$$\varepsilon'' = \frac{\sigma}{\omega\varepsilon_0} \tag{6}$$

where ε_0 is the vacuum permittivity (8.85×10^{-12} F/m), and ω is the angular frequency.

Therefore, the loss tangent can also be expressed as:

$$\tan\delta = \frac{\sigma}{\omega\varepsilon_0\varepsilon'} \tag{7}$$

For a single, homogeneous dielectric material, the dielectric loss can be calculated directly from the real and imaginary parts of the complex permittivity. However, in finite element simulations, the equivalent dielectric loss of the entire bushing or a specific region is often obtained by field-quantity integration. Under a sinusoidal time-varying electric field with angular frequency ω and electric field magnitude E, energy loss occurs in the dielectric material due to polarisation relaxation or leakage conduction. The average power loss per unit volume is:

$$Q_{\text{loss}} = \frac{1}{2}\omega\varepsilon''|E|^2 = \frac{1}{2}\sigma|E|^2 \tag{8}$$

The average stored energy per unit volume is:

$$W_{\text{e}} = \frac{1}{4}\varepsilon'|E|^2 \tag{9}$$

Substituting Equations (7) and (8) into Equation (4) yields:

$$\tan\delta = \frac{2Q_{\text{loss}}/\omega|E|^2}{4W_{\text{e}}/|E|^2} = \frac{Q_{\text{loss}}}{2\omega W_{\text{e}}} \tag{10}$$

For nonuniform regions or composite materials, the equivalent dielectric loss is calculated using the volume-average integration:

$$\tan\delta = \frac{\int_{V_{\text{sel}}} Q_{\text{loss}}dV}{2\omega\int_{V_{\text{sel}}} W_{\text{e}}dV} \tag{11}$$

where V_{sel} is the selected integration region, which can be implemented using the integration operator or volume integration function.

2.3. Full-Scale Model Simulation of the Normal Bushing

All finite element simulations in this work were performed using COMSOL Multiphysics® version 6.4. To carry out the simulation analysis of defective bushings, a full-scale normal bushing model was first constructed based on the geometric structure parameters, and the material properties and boundary conditions were subsequently set. A multi-region adaptive meshing strategy was adopted. Regions with steep electric field gradients, such as the condenser core and local defect areas, were refined with tetrahedral elements, while regions with gentle field variations, such as the external air domain and porcelain sheds, were assigned relatively coarse meshes to balance accuracy and efficiency. The final full-scale mesh contains 4,272,232 mesh vertices and 25,465,160 domain elements in total.

Based on the structural dimensions of a true-type 35 kV oil-impregnated paper bushing, the total length is 1440 mm, the conductor rod is 1120 mm long, and it has an inner diameter of 36 mm and an outer diameter of 45 mm. The maximum diameter of the upper porcelain shed is 260 mm, with a length of 485 mm; the flange length is 115 mm, and the lower porcelain length is 355 mm. The insulation structure of the bushing is the condenser core, formed by alternately winding aluminium foil and insulating paper around the central conductor. The aluminium foil thickness is 0.007 mm. The outermost aluminium foil is connected to the grounding terminal of the flange, serving as the earthed electrode plate. The structural dimensions of the 35 kV bushing condenser core are listed in Table 1.

Table 1. Structural dimensions of the 35 kV bushing condenser core.

Layer	Foil Length/mm	Paper Layers	Upper Deviation/mm	Lower Deviation/mm
Conductor rod	/	/	/	/
1	732	4	/	/
2	689	4	33	10
3	646	4	33	10
4	603	5	33	10
5	560	5	33	10
6	517	5	33	10
7	474	5	33	10
8	431	4	33	10
9	388	4	33	10
10	345	4	33	10
Protection	86	/	/	/

Based on the actual geometric parameters in Table 1, taking the relative permittivity of oil-impregnated paper as $\varepsilon_r = 4.2$, the inter-layer capacitances of the 10 main insulation layers were calculated layer by layer, according to the above formula. After series equivalent calculation, the theoretical main-screen capacitance is about 230 pF. This calculation only considers the main radial inter-layer capacitance of the condenser core, adopts the ideal concentric cylinder approximation, and ignores end edge effects and axial electric field distortion.

The full-scale three-dimensional model of the bushing includes key external structures, such as the tank, oil conservator, upper porcelain, lower porcelain, metal flange, and grading ring. To accurately calculate the electric field distribution, a cylindrical structure is added around the entire bushing to form a closed air domain enclosing the bushing. At the same time, a thin layer on the periphery of the air domain is set as a virtual domain to expand the computational range of the air domain, thereby improving the accuracy of the simulation results. The three-dimensional model of the full-scale bushing is shown in Figure 1.

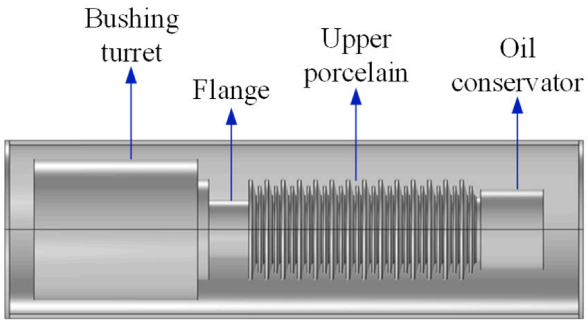


Figure 1. A three-dimensional model of the full-scale bushing.

In the boundary condition and material parameter settings of the bushing model, the central conductor rod is set as the voltage-carrying element, with a high-voltage potential of 35 kV applied; the boundary of the air domain is set to zero charge, i.e., an electric potential of 0; and the outermost capacitive screen is connected to the flange and earthed, also with a potential of 0. To simplify the calculation, the thickness of the aluminium foil electrodes in the condenser core is neglected, and they are set to floating potential. Under power-frequency AC voltage, the material parameters for each region are set as shown in Table 2.

Table 2. The dielectric parameters of the materials in each region of the bushing.

Material	Relative Permittivity	Conductivity/(S/m)
Copper	1	5.998×10^{7}
Aluminium foil	1	3.774×10^{7}
Oil-impregnated paper	4.2	4×10^{-11}
Transformer oil	2.2	3×10^{-13}
Porcelain	3.75	1×10^{-14}

Subsequently, mesh generation and simulation analysis were performed on the full-scale bushing model, and the simulation results of the normal bushing were obtained at a room temperature of 25 °C and a power-frequency 50 Hz voltage excitation. All simulations were run on a workstation equipped with an Intel Xeon Silver 4114 CPU (Intel Corporation, Santa Clara, CA, USA) @ 2.20 GHz and 96 GB of RAM. For the power-frequency (50 Hz) steady-state simulation, the total number of degrees of freedom (DOFs) for the solution is 33,827,382; the total time from equation compilation and variable initialisation to convergence is approximately 55 min per frequency point. For defective models with locally refined meshes, the solution time slightly increases with the complexity of the defect structure, generally ranging from 55 to 60 min.

From the potential distribution, it can be observed that the central conductor rod is the high-potential terminal with the highest electric potential. The upper part of the bushing, which is in direct contact with the transformer oil and connected externally to the oil conservator, forms a high-potential region. The lower part of the conductor rod, also in contact with the transformer oil, forms another high-potential region. The middle section, where the flange and the outermost capacitive screen are earthed, exhibits a low potential. Overall, the axial potential distribution shows a trend of high values at both ends and low values in the middle, while the radial potential gradually decreases from the central conductor rod outward. The potential and electric field distributions of the normal bushing are shown in Figure 2.

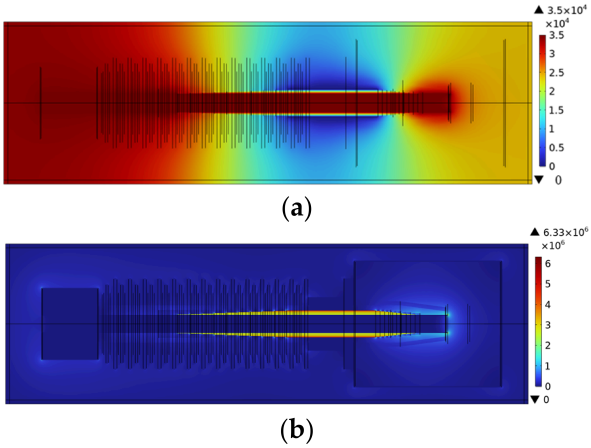


Figure 2. The electric field and potential distributions of the normal bushing: (**a**) the potential distribution of the normal bushing and (**b**) the electric field distribution of the normal bushing.

Given the respective strengths of the electrostatics and electric currents solution models in calculating the dielectric parameters of bushings, the electrostatics module and the electric currents module are used separately to solve for the bushing capacitance and dielectric loss factor, respectively. The dielectric characteristic parameters of the full-scale normal bushing were calculated and are listed in Table 3.

Table 3. Dielectric parameters of the normal bushing.

Parameter 50.	Bushing Parameters
Frequency/Hz	50
Volume loss density/W	0.15
Time-average electric energy density/J	0.07
Capacitance value/pF	241.37
Dielectric loss	0.32%

The simulated main-screen capacitance is 241.37 pF, with a relative deviation of approximately 4.9% from the theoretical value. The main error sources are as follows: the theoretical formula only calculates the interlayer main capacitance of the capacitor core, whereas the full-scale simulation model includes the stray capacitances introduced by the fringing electric field at the ends of the capacitor screens, the porcelain housing, the flange, and the end of the conductor rod, as well as the oil domain and air domain. In addition, the theoretical formula assumes that the screen layers are ideal coaxial cylinders, while the actual simulation model incorporates real geometric features, such as the axial stepped structure of the foil layers and the end contours, so that the electric field distribution is closer to the actual operating condition. This deviation is within the conventional acceptable range for high-voltage insulation engineering, and the two values are reasonably consistent at the engineering level. The dielectric loss factor is 0.32%. These dielectric parameters of the normal bushing were used as the baseline reference for analysing the influence mechanisms and patterns of various defects on the bushing.

3. Simulation Calculation of Typical Defective Bushing Models

3.1. Electrode Defect Models of the Bushing

1. Sawtooth defects on the foil electrodes

To simulate typical physical defects that may occur during the manufacturing process of the condenser core, such as uneven edges, local damage, and interlayer misalignment of the aluminium foil electrodes, a continuous sawtooth structure with a length of 20 mm was arranged on the upper edge of the first main electrode plate of the condenser core in the full-scale bushing model, so as to characterise the local electric field distortion induced by abnormal electrode plate structures. This artificially introduced sawtooth defect on the foil simulates the irregular edge conditions encountered in actual manufacturing processes, thereby enabling the study of its impact on the insulation performance of the bushing. The simulation method for this defect structure is shown in Figure 3.

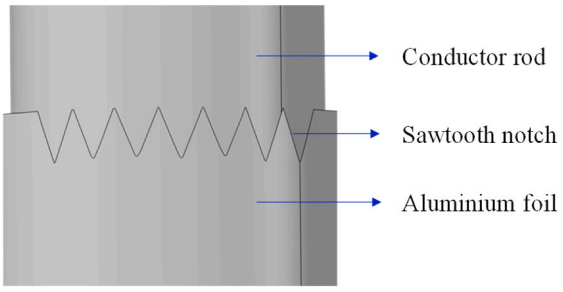


Figure 3. The simulation of sawtooth defects on the bushing foil.

Under power-frequency voltage, the electric field distributions at the foil edges of the normal and defective bushings were obtained through simulation. The results show that under the normal condition, the field distribution at the foil edges is relatively smooth,

with a maximum field strength of 1.73 kV/mm, reflecting the field-grading effect of the condenser core. When sawtooth defects are present at the foil edges, a pronounced tip effect occurs, significantly increasing the local maximum field strength to 3.54 kV/mm, a distortion increase of 104.62%. A comparison of the electric field distributions at the foil edges of the normal and defective bushings is shown in Figure 4. Such field distortion not only significantly reduces the partial discharge inception voltage of the bushing insulation but also, in combination with insulation degradation, can readily lead to thermal breakdown or flashover events in the insulation system.

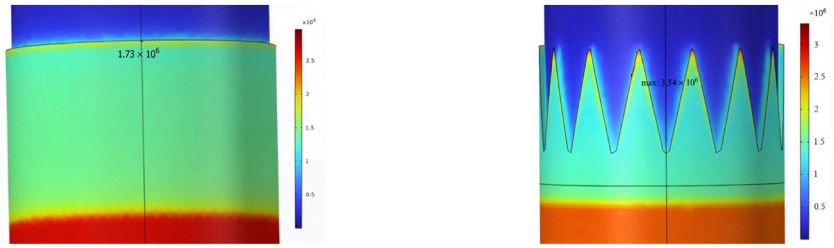


Figure 4. Electric field distributions at the foil edges of the normal and defective bushings: (**a**) the normal bushing and (**b**) the bushing with the sawtooth foil defect.

2. Metallic tip defects between foils

To simulate the presence of metallic foreign particles between the foil layers, three copper wires with a diameter of 0.4 mm and a length of 20 mm were fixed between the first and second capacitor screens. Their tip structures can effectively simulate the metallic burrs or residual conductors that may appear in actual operation. This region is prone to local electric field concentration, thereby generating high field strengths. The simulation method for this defect is shown in Figure 5.

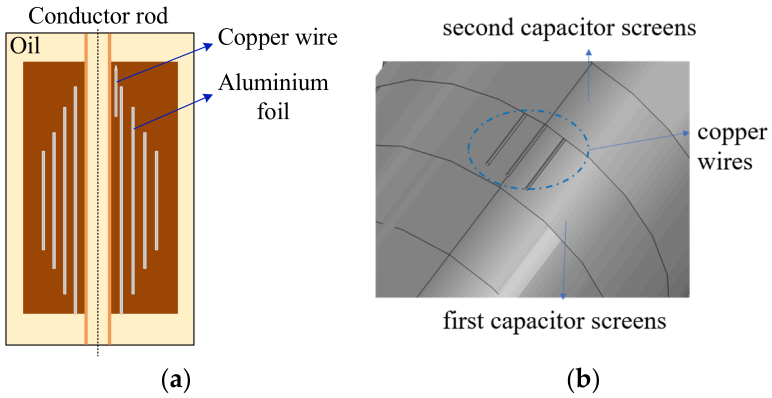


Figure 5. The simulation method for metallic tip defects between foils: (**a**) a schematic of the tip defect and (**b**) the simulation model of the metallic tip defect.

Under power-frequency AC voltage, the electric field distribution of this defect model was obtained through simulation. The insertion of the copper wire between the conductor rod and the first screen significantly alters the original field distribution in this region, leading to a degradation of the insulation performance of the condenser core. Meanwhile, a pronounced field concentration effect occurs at the tip and edges of the copper wire, with the maximum electric field strength reaching 17.51 kV/mm. The electric field distribution of the metallic tip defect between foils is shown in Figure 6. Such localised high-field regions are highly prone to partial discharge, posing a threat to the long-term safe operation of the bushing.

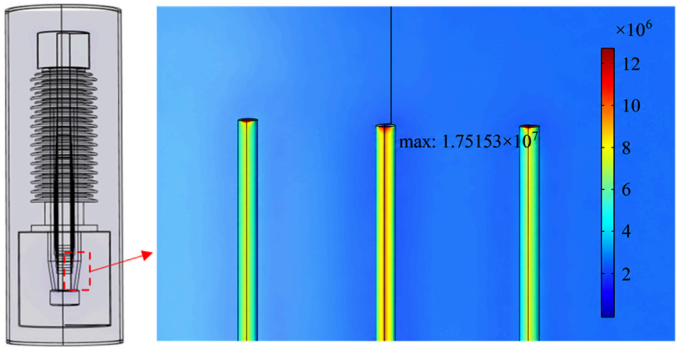


Figure 6. The electric field distribution of the metallic tip defect between foils.

Using global calculation and volume integration methods, the dielectric characteristic parameters of the metallic tip defect model were obtained, and the results are presented in Table 4. Similar to the creepage defect on the lower porcelain, although this defect causes slight changes in the internal capacitance and dielectric loss of the bushing, its overall influence remains very weak.

Table 4. Dielectric parameters of the bushing with metallic tip defects between foils.

Parameter Type	Bushing Parameters
Frequency/Hz	50
Volume loss density/W	0.15
Time-average electric energy density/J	0.07
Capacitance value/pF	241.32
Dielectric loss	0.34%

3.2. The Insulation Defect Model of the Lower Porcelain of the Bushing

To simulate the insulation defect on the inner wall of the lower porcelain housing, a rectangular copper foil of approximately 5 cm × 10 cm was attached to the high-field longitudinal region on the inner wall of the lower porcelain housing, with the foil in close contact with the inner wall and one end in contact with the flange. This configuration effectively simulates metallic foreign objects or local field concentration sources that may occur on the inner insulation surface of the lower porcelain in actual operation. The setup method for the creepage defect on the lower porcelain is shown in Figure 7.

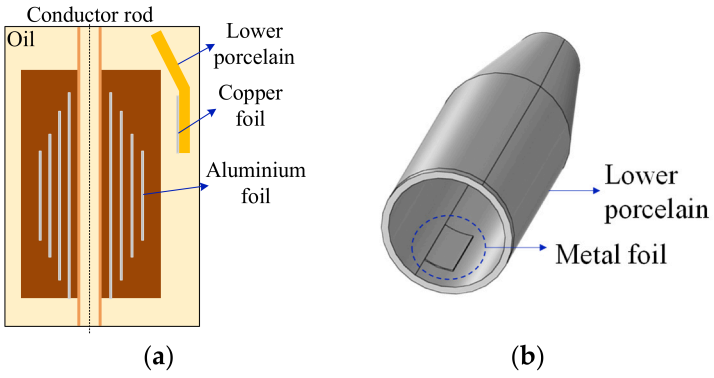


Figure 7. The configuration of the creepage defect on the internal surface of the lower porcelain: (**a**) a schematic of the tip defect and (**b**) a simulation model of the metallic tip defect.

Under power-frequency AC voltage, the metal foil is connected to the flange and, therefore, has zero potential. The simulated electric field distribution shows that a pronounced

field distortion and concentration occur at the edges of the metal foil, with the local field strength significantly increased and a maximum value of 8.92 kV/mm. This field concentration effect caused by the sharp edges of the metal foil is prone to induce discharge, posing a potential threat to the internal insulation of the bushing. The electric field distribution at the copper foil on the inner wall of the lower porcelain is shown in Figure 8.

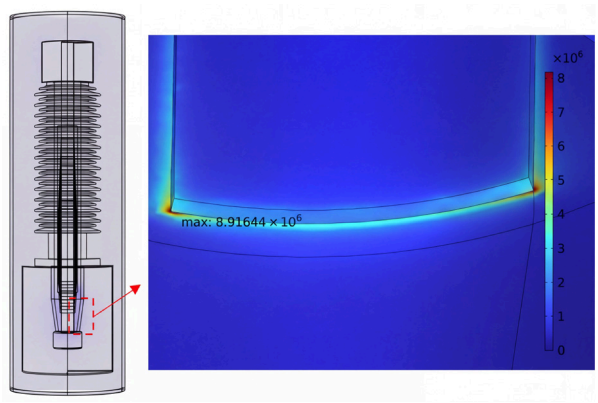


Figure 8. The electric field distribution at the copper foil inside the lower porcelain.

Further calculation of the dielectric characteristic parameters of this defect model reveals that, compared with the normal bushing, the creepage defect on the lower porcelain has only a weak influence on the capacitance and dielectric loss values. The calculated results are listed in Table 5. This is because the defect is localised in nature, while capacitance and dielectric loss parameters are primarily sensitive to changes in the overall insulation condition and are, therefore, insufficient to effectively reflect the presence of localised defects.

Table 5. Dielectric parameters of the bushing with the creepage defect on the lower porcelain.

Parameter Type	Bushing Parameters
Frequency/Hz	50
Volume loss density/W	0.15
Time-average electric energy density/J	0.08
Capacitance value/pF	242.25
Dielectric loss	0.33%

3.3. End-Screen Grounding Loss Defect Model

In transformer bushings, the end-screen lead structure is typically delicate, consisting of a thin metal rod or spring contact that extends from the bushing base and is connected to the ground wire via a small ground bushing or dedicated terminal. Owing to its low mechanical strength, contact loosening, displacement, or even jamming may occur during installation, maintenance, or long-term vibration during operation. In addition, a sealing ring is usually provided at the end-screen lead terminal; after prolonged operation, the sealing ring may age and lose elasticity, allowing moisture ingress, which leads to oxidation and corrosion of the end-screen lead rod and the inner wall of the ground bushing, resulting in a sharp increase in contact resistance. Meanwhile, the copper ground wire or connectors exposed to the atmosphere may also suffer from electrochemical corrosion and fracture. Any of these factors can cause poor grounding or even complete loss of grounding of the end screen, leaving it in a fully floating state. To simulate this fault, the boundary condition of the end screen was set to completely floating, representing the end-screen wire breakage and grounding loss caused by various reasons. The defect simulation method is illustrated in Figure 9.

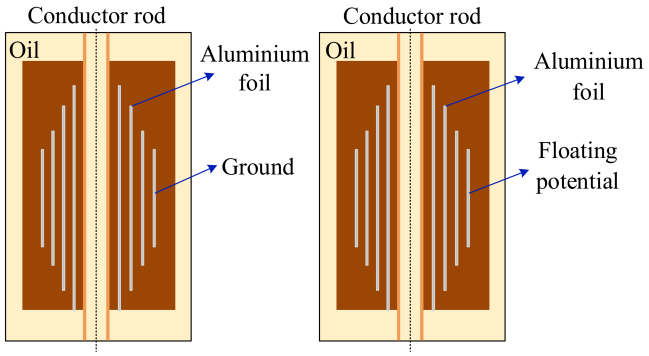


Figure 9. The simulation method for the end-screen grounding loss defect.

In the case of the end-screen grounding loss, the end screen and the flange form a pair of electrodes, with the intervening insulating oil serving as the dielectric medium, thereby constituting an equivalent capacitance. This capacitance is much smaller than the main-screen capacitance of the condenser core. Since the main-screen capacitance and the end-screen capacitance are connected in series, according to the principle of series capacitive voltage division, a relatively high voltage will be applied across the end screen and the flange, consequently generating a strong electric field. Moreover, the breakdown strength of the insulating oil is lower than that of the oil-impregnated paper, making this region more susceptible to partial discharge or even insulation breakdown. The electric field distribution of the bushing with end-screen grounding loss is shown in Figure 10, where a strong electric field exists between the end screen and the flange. The electric field and potential distributions along the central axial line of the condenser core are shown in Figure 11.

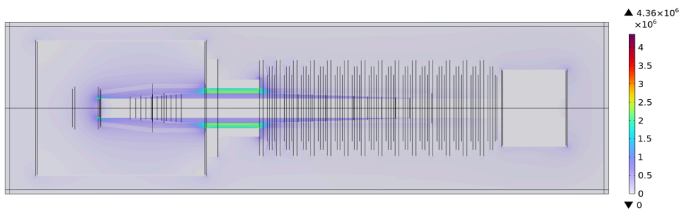


Figure 10. The electric field distribution of the bushing with end-screen grounding loss.

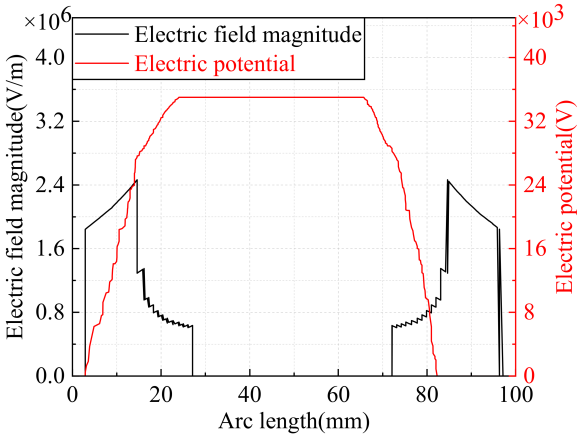


Figure 11. The electric field and potential distributions along the central axial line.

Under the grounding-loss condition, the voltage on the end screen reaches approximately 26 kV, which is significantly higher than the distributed voltage of about 9 kV on each layer of the condenser core. Meanwhile, the electric field strength in the insulating oil in this

region reaches 2.40 kV/mm, markedly exceeding the maximum field strength in the layers of the condenser core (approximately 1.30 kV/mm at the outermost layer). Owing to the relatively low breakdown strength of the insulating oil, this fault can easily lead to bushing breakdown and overall insulation failure. The dielectric characteristic parameters of the end-screen grounding loss defect, obtained by integral calculation, are listed in Table 6. As the main and end screens are in series, the overall insulation capacitance of the bushing decreases significantly under the end-screen grounding loss condition, accompanied by a substantial reduction in the dielectric loss factor.

Table 6. Dielectric parameters of the bushing with the end-screen grounding loss.

Parameter Type	Bushing Parameters
Frequency/Hz	50
Volume loss density/W	0.01
Time-average electric energy density/J	0.02
Capacitance value/pF	62.84
Dielectric loss	0.08%

4. Preparation of Typical Defective Bushings

4.1. Simulation of Electrode Manufacturing Defects

To investigate the manufacturing defects of bushing electrodes, this study simulated two types of defects: sawtooth defects at the edges of the aluminium foil electrodes and metallic tip defects between the electrode layers. During the winding process of the condenser core, these defects were artificially introduced through physical means to study their effects on insulation characteristics. To simulate mechanical damage caused during bushing manufacturing, a sawtooth notch with a length of 20 mm was fabricated on the upper edge of the first main electrode plate of the condenser core, forming a local electric field concentration zone to simulate the partial discharge characteristics induced by electrode tip distortion. To simulate metallic impurities that may be introduced during manufacturing and assembly, three copper wire tips were fixed between the first and second electrode layers to simulate the electric field distortion and typical discharge signals caused by metallic impurities. The simulation methods for the sawtooth foil defect and the metallic tip defect between electrode layers are shown in Figures 12 and 13, respectively.

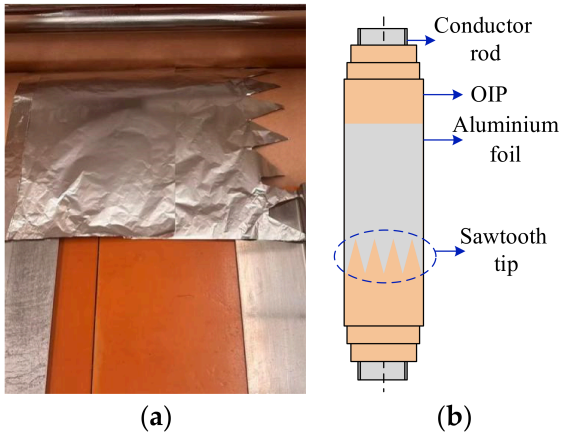


Figure 12. The simulation of the sawtooth defects on the bushing foil: (**a**) the sawtooth foil electrode and (**b**) the foil electrode defect.

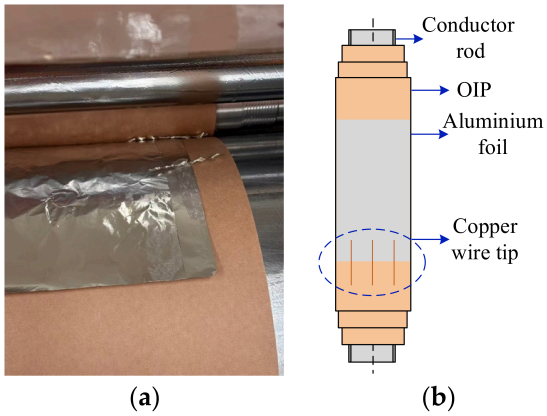


Figure 13. The simulation of the metallic tip defects between the foils of the bushing: (**a**) the electrode plate with copper wire tips and (**b**) a schematic of the copper wire tips.

4.2. The Simulation of the Creepage Defects on the Lower Porcelain

Creepage defects on the inner insulation surface of the lower porcelain mainly arise from sealing failure and surface contamination accumulation. To simulate this defect, a rectangular copper foil of approximately 5 cm × 10 cm was firmly attached with conductive adhesive to the top longitudinal region of the inner wall of the lower porcelain, where the electric field is relatively high and contamination is prone to accumulate, before final assembly. This arrangement simulates the creepage path caused by foreign matter attachment or surface pollution. The simulation of the creepage defect on the internal surface of the lower porcelain is shown in Figure 14.

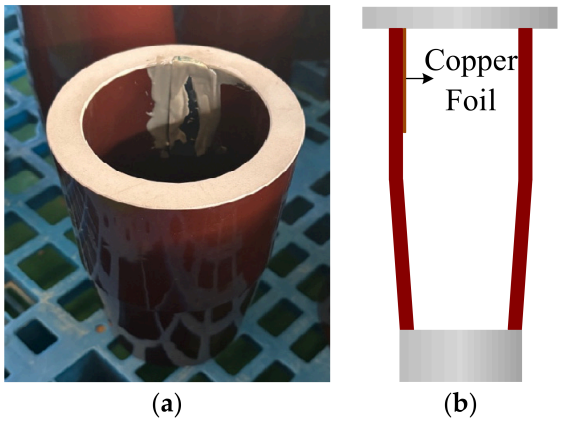


Figure 14. The simulation of the creepage defect on the internal surface of the lower porcelain. (**a**) The copper foil on the inner wall of the lower porcelain and (**b**) a schematic of the creepage defect.

4.3. Simulation of End-Screen Grounding Loss

End-screen grounding loss is usually caused by manufacturing process defects or long-term operational ageing. To simulate this common operational defect, the reliable electrical connection between the end-screen lead and the ground terminal was deliberately disconnected, leaving the end screen in a floating potential state and prone to intermittent discharge.

5. Testing and Analysis of Defective Bushings

5.1. Dielectric Characteristics of Typical Defective Bushings

Dielectric loss and capacitance measurements were performed on the defective bushings using an HD7000A variable-frequency, anti-interference dielectric loss tester manufac-

tured by Yangzhou Huadian Electric Co., Ltd., Yangzhou, China. For the main-screen capacitance measurement, the normal connection method was adopted, with the high-voltage terminal of the tester connected to the conductor rod of the bushing and the measured capacitance terminal connected to the end-screen terminal. At an ambient room temperature of approximately 25 °C, power-frequency voltage levels of 2 kV, 5 kV, and 10 kV were applied, and dielectric loss and main-screen capacitance measurements were conducted on the normal bushing and bushings with different defect types. The test results are also shown in Figure 15.

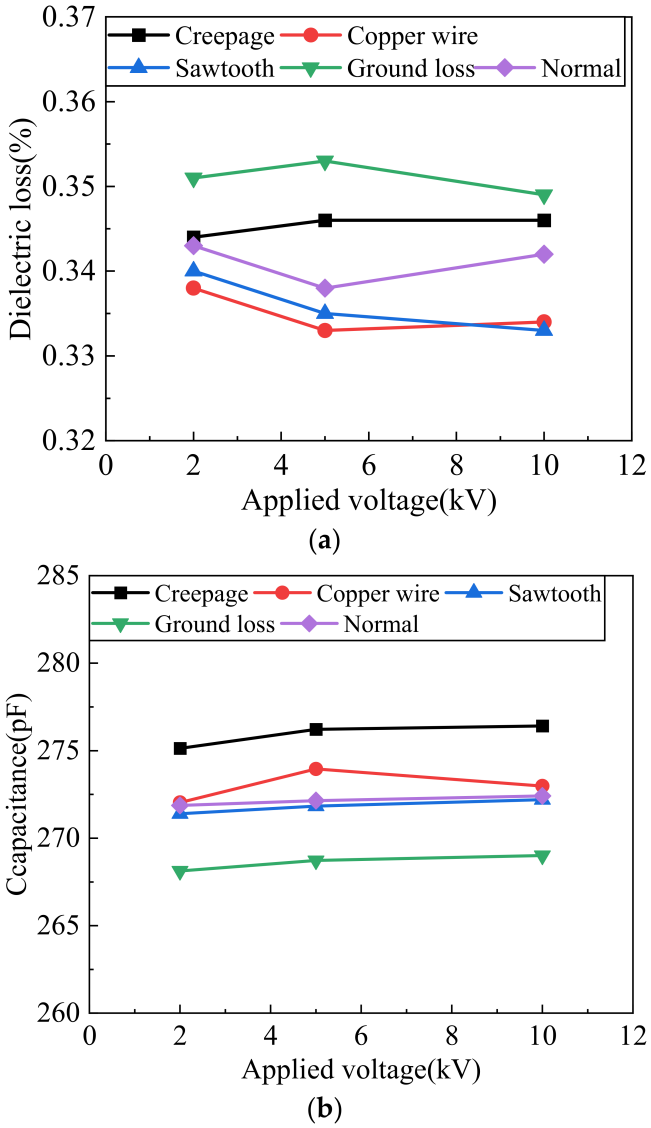


Figure 15. The test results of the dielectric loss and capacitance of the main screen of the bushing: (**a**) the dielectric loss of the main screen of the bushing and (**b**) the capacitance of the main screen of the bushing.

The simulated dielectric loss factor of the normal bushing is 0.32%, and the experimentally measured value is 0.34%, with a relative deviation of about 5.9%. This deviation mainly comes from the homogeneous idealised assumption of insulating material parameters in the simulation, which does not take into account factors such as trace impurities in actual insulating paper and differences in impregnation uniformity. The overall deviation is within the acceptable range for engineering applications, which verifies the reliability of the dielectric loss calculation of the simulation model.

5.2. Partial Discharge Characteristics of Typical Defective Bushings

The PD test platform for oil-impregnated paper (OIP) condenser bushings primarily consists of a power-frequency high-voltage source, a high-frequency current transformer (HFCT), and an oscilloscope, as shown in Figure 16. During the tests, the power-frequency high-voltage source, comprising a test transformer and a capacitive voltage divider, was used to apply AC power-frequency high voltage to the bushing. An HFCT model 60V2 was employed to detect the PD signals from the bushing.

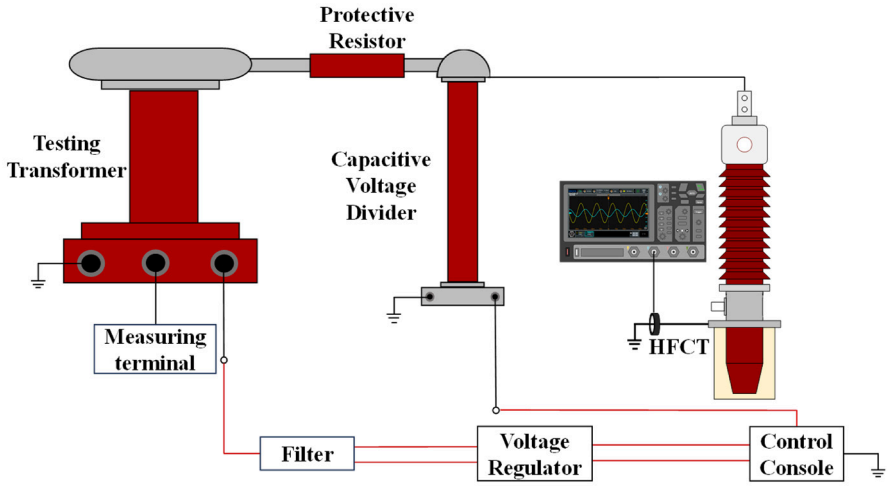


Figure 16. The partial discharge test setup for the bushings.

A step-by-step voltage boosting method was adopted in this experiment to investigate the PD characteristics and evolution patterns of bushings with different defect types. It is essential to accurately determine the PDIV prior to PD measurement. After the waveform stabilised, the voltage was raised stepwise from 0 kV at a constant step size until continuous and repetitive PD pulses were detected for the first time. The voltage applied at that moment was recorded as the PDIV. The test results are shown in Figure 17.

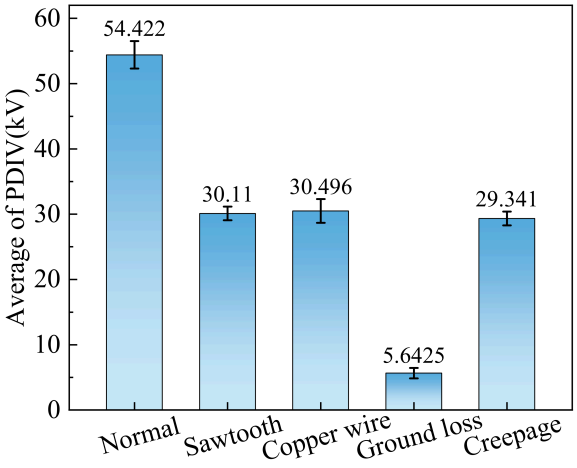


Figure 17. PDIV measurements of normal bushing and bushings with different defects.

5.3. Analysis of Insulation Characteristics of Typical Defective Bushings

When sawtooth notches are present on the foil electrodes, the smoothness of the foil edges is disrupted, resulting in a markedly reduced radius of curvature and severe local electric field distortion, producing an extremely strong field enhancement effect. Near the voltage peak, the field strength at the tip region first breaks down the adjacent transformer

oil, thereby initiating partial discharge. The sawtooth defect on the foil electrodes causes highly nonuniform and intense edge field distortion at the notch, further reducing the PDIV to 35 kV. When a copper wire tip exists between the foil electrodes, this metallic conductor remains at a floating potential within the insulation layer, effectively acting as an isolated floating electrode introduced between the two adjacent foils of the condenser core. This floating electrode couples with the adjacent foils through parasitic capacitances, and its equivalent potential depends on the capacitive voltage division ratio and its relative position to the foils. When the potential difference between the floating electrode and one of the foils exceeds the withstand strength of the intervening oil-paper insulation, spark discharge occurs.

The presence of a copper foil attached to the internal surface of the lower porcelain alters the equipotential distribution in that region, reducing the electric field component normal to the insulation surface while significantly increasing the tangential component parallel to the surface. The PDIV of the bushing with the creepage defect is approximately 30 kV.

As the outermost foil layer of the condenser bushing, the end screen is intended to provide a reliable ground connection for the outermost section of the condenser core. When the end screen loses its ground connection, the entire condenser core effectively forms a capacitive voltage divider structure with respect to ground. Specifically, the series capacitive layers of the condenser core divide the voltage to ground, and the voltage across the small air gap between the end screen and the flange is determined by the voltage division ratio between the gap capacitance and the equivalent capacitance of the entire core. Although the distance between the end screen and the flange is very small, typically only a few millimetres, the large surface area of the end screen allows substantial charge accumulation, resulting in an extremely high potential difference across this small gap and consequently causing intense spark discharge in the air or insulating medium. This discharge is essentially a floating-potential discharge, characterised by high energy and strong destructive effects. Each discharge event causes local ablation on the surfaces of both the end screen and the flange, and prolonged operation may lead to cumulative insulation degradation and even breakdown.

Owing to the ungrounded end screen, the small capacitive gap between the end screen and the flange can be broken down by the divided voltage even at relatively low test voltages, resulting in an extremely low PDIV of approximately 6 kV.

The power-frequency test results show that the end-screen grounding loss defect has the most significant impact on the overall dielectric parameters of the bushing, with obvious differences in both capacitance and dielectric loss compared with the normal bushing. In contrast, the sawtooth defect, metallic tip defect, and internal creepage defect are all localised defects, and their influences on the overall capacitance and dielectric loss are very limited. In terms of partial discharge characteristics, all four types of defects induce local electric field distortion, resulting in varying degrees of reduction in the partial discharge inception voltage (PDIV). Among them, the PDIV of the end-screen grounding loss decreases the most, followed by the internal creepage defect, and the PDIVs of the metallic tip and sawtooth defects are also significantly lower than that of the normal bushing.

6. Conclusions

For the four typical defects of 35 kV OIP condenser bushings, namely sawtooth defects on the foil electrodes, metallic tips between foils, creepage on the internal surface of the lower porcelain, and end-screen grounding loss, a systematic investigation of the electric field distribution, dielectric response, and PD characteristics was conducted through full-

scale three-dimensional simulations and experimental tests on defective specimens. The main conclusions are as follows:

1. Both sawtooth defects on the foil electrodes and metallic tips between the foils exhibit a significant tip effect, with maximum field strengths reaching 3.54 kV/mm and 17.51 kV/mm, respectively. The field strength at the sawtooth defect is 104.62% higher than that of the normal structure. Both types of defects have a negligible effect on the power-frequency capacitance, dissipation factor, and frequency-domain dielectric spectrum, but significantly reduce the PDIV.
2. The creepage defect on the internal surface of the lower porcelain causes a field concentration at the edge of the metal foil, with a maximum field strength of 8.92 kV/mm. The overall dielectric parameters show limited variation, while the PDIV decreases, indicating that local field distortion is the primary manifestation of insulation degradation.
3. End-screen grounding loss raises the end-screen potential to approximately 26 kV, and the field strength in the adjacent insulating oil reaches 2.40 kV/mm, which is higher than the maximum field strength in the outermost layer of the condenser core (1.30 kV/mm). The measured capacitance and dissipation factor change significantly, consistent with the potential redistribution observed in the simulation.
4. The simulation and experimental results corroborate each other. However, owing to the limited number of specimens and the specific defect severity settings, further research involving multiple sizes, composite defects, and multiphysics field coupling conditions is required in future work.

Author Contributions: Conceptualization, J.Z. and T.W.; methodology, J.Z. and Y.L.; software, P.W. and J.J.; validation, Y.L. and J.J.; formal analysis, J.Z. and P.W.; investigation, Y.L. and P.W.; resources, T.W. and Y.L.; data curation, J.J. and P.W.; writing—original draft preparation, J.Z.; writing—review and editing, T.W. and J.J.; visualization, P.W.; supervision, T.W.; project administration, T.W.; funding acquisition, T.W. All authors have read and agreed to the published version of the manuscript.

Funding: This research was supported by the Science and Technology Project of State Grid Jiangsu Electric Power Co., Ltd. (Grant No. J2025074).

Data Availability Statement: The original contributions presented in this study are included in the article. Further inquiries can be directed to the corresponding author.

Conflicts of Interest: Authors Yuandi Lin, Tonglei Wang, and Peng Wu were employed by the company State Grid JiangSu Electric Power Company. The remaining authors declare that the research was conducted in the absence of any commercial or financial relationships that could be construed as potential conflicts of interest. The authors declare that this study received funding from State Grid Jiangsu Electric Power Co., Ltd. The funder was not involved in the study design, collection, analysis, interpretation of data, the writing of this article or the decision to submit it for publication.

References

1. Hu, Z.Y.; Li, Z.; Chen, H.W.; Lu, X. Transformer condition detection and evaluation method based on voiceprint compression and cost-sensitive learning. *Electr. Power Eng. Technol.* **2024**, *43*, 209–216. (In Chinese)
2. Yang, H.; Hu, W.X.; Zhang, L.; Chen, J.; Zhou, S.; Zhao, S. Fault diagnosis of transformer oil-paper bushings in PSO-BPNN algorithm based on ADASYN data balancing. *Electr. Power Eng. Technol.* **2024**, *43*, 170–178. (In Chinese)
3. Qi, B.; Dai, Q.; Li, C.; Zeng, Z.; Fu, M.; Zhuo, R. The mechanism and diagnosis of insulation deterioration caused by moisture ingress into oil-impregnated paper bushing. *Energies* **2018**, *11*, 1496. [CrossRef]
4. Dong, B.B.; Li, B.H.; Li, J.S. Multi-source partial discharge ultrasonic hybrid pulse recognition method for oil-paper insulation defects. *Electr. Power Eng. Technol.* **2025**, *44*, 176–187. (In Chinese)
5. Dong, B.B.; Li, B.H.; Gao, C.S. UHF anti-interference positioning and optimal layout method of oil-paper insulation defect partial discharge. *Electr. Power Eng. Technol.* **2024**, *43*, 181–191. (In Chinese)
6. Goh, H.H.; Yin, J.; Zhang, Y.; Wei, W.; Su, Z.; Wang, G. Study on lifespan prediction of oil-paper bushing considering the influence of moisture-accelerated aging. *IEEE Trans. Dielectr. Electr. Insul.* **2022**, *30*, 458–465. [CrossRef]

7. Tian, W.; Zhang, D.; Yao, H.; Xu, H.; Xu, P.; Yang, D.; Zhang, G. Temperature normalisation and moisture assessment of oil-paper insulation based on dielectric response in extremely cold conditions. *High Volt.* **2025**, *10*, 903–916. [CrossRef]
8. Shi, S.; Hao, J.; Zeng, Q.; Yin, F.; Liao, R. Moisture and aging degree evaluation method for oil-paper insulation based on HV-FDS characteristics analysis. *IEEE Trans. Dielectr. Electr. Insul.* **2024**, *31*, 2520–2530. [CrossRef]
9. Liang, Z.; Sun, Y.; Cheng, H.; Zhang, N.; Li, B.; Liu, Y.; Fang, Y.; Zhang, Y. A comprehensive evaluation method for moisture and aging state of oil-immersed paper bushings based on dielectric modulus and K-nearest neighbor algorithm. *Front. Energy Res.* **2024**, *11*, 1348433. [CrossRef]
10. Firuzi, K.; Vakilian, M.; Phung, B.T.; Blackburn, T.R. Partial discharges pattern recognition of transformer defect model by LBP & HOG features. *IEEE Trans. Power Deliv.* **2019**, *34*, 542–550. [CrossRef]
11. Jiang, J.; Chen, J.; Li, J.; Yang, X.; Bie, Y.; Ranjan, P.; Zhang, C.; Schwarz, H. Partial discharge detection and diagnosis of transformer bushing based on UHF method. *IEEE Sens. J.* **2021**, *21*, 16798–16806. [CrossRef]
12. Hao, Z.; Jiang, C.M.; Li, H. High-frequency partial discharge monitoring technology based on TAs in transformer bushing risers. *High Volt. Eng.* **2025**, *51*, 1126–1134. (In Chinese)
13. Wang, Q.Y.; Yang, X.; Peng, Z.R.; Liu, P. 3D coupled electromagnetic-thermal-fluid method for computation of temperature field of converter transformer RIP bushings. *Proc. CSEE* **2016**, *36*, 6269–6275. (In Chinese)
14. Illias, H.; Chen, G.; Lewin, P.L. Partial discharge behavior within a spherical cavity in a solid dielectric material as a function of frequency and amplitude of the applied voltage. *IEEE Trans. Dielectr. Electr. Insul.* **2011**, *18*, 432–443. [CrossRef]
15. Zhao, X.; Hu, J.; Yuan, Z.; He, J. Design of adaptive bushing based on field grading materials. *High Volt.* **2021**, *6*, 625–636. [CrossRef]
16. Li, J.; Wang, D.; Sun, C.H.; Sun, Y.D.; Xu, R. Study on temperature rise characteristics and influence law of GIS basin-type insulator. *Shandong Electr. Power Technol.* **2025**, *52*, 104–112. (In Chinese)
17. Chen, L.; Wu, X.; Tian, Y.; Long, Z.; Su, C.; Lin, T.; Liu, R. PD defect monitoring for oil-impregnated paper bushing by measuring the inner pressure. *IEEE Access* **2019**, *7*, 53411–53418. [CrossRef]
18. Zhang, G.Z.; Lu, C.Y.; Zhou, H.; Tian, H.L.; Yu, X.; Zhang, X. Integrated acoustic and UHF sensing technology for partial discharge of power equipment. *High Volt. Eng.* **2022**, *48*, 5090–5101. (In Chinese)
19. Judd, M.D.; Yang, L.; Hunter, I.B.B. Partial discharge monitoring of power transformers using UHF sensors. Part I: Sensors and signal interpretation. *IEEE Electr. Insul. Mag.* **2005**, *21*, 5–14. [CrossRef]
20. Taghizade Ansari, H.; Vahedi, A.; Mahmoudi, N. Evaluating the insulation condition of oil-impregnated paper bushings based on the time constant database. *IET Electr. Power Appl.* **2024**, *18*, 1233–1243. [CrossRef]
21. Zhao, C.M.; Si, C.J.; Guo, J.C.; Yang, D.Y.; Li, S.J.; Yu, M.H. Study on the variation law of electric field distribution/distortion characteristics of 220 kV oil-immersed bushing under typical faults. *Insul. Mater.* **2025**, *58*, 131–140. (In Chinese)
22. Si, W.R.; Fu, C.Z.; Su, L.; He, L.; Wen, H.; Jiang, Y.; Li, J. Research on electric field distribution characteristics simulation under typical defects in the scaled model of valve side bushing of UHV converter transformer. *High Volt. Appar.* **2024**, *60*, 85–94. (In Chinese)
23. Fan, X.; Li, S.; Sun, T.; Zhang, Y.; Liu, J. Moisture evaluation of oil-immersed insulation in bushings based on frequency domain spectroscopy and grey relational analysis. *CSEE J. Power Energy Syst.* **2025**, *11*, 909–918.
24. Wang, L.J.; Fang, C.X.; Yang, H.T.; Wu, X.; Hu, X.; Wu, J. Calibration simulation of UHF sensor for GIS partial discharge based on S11 and S21 cross-comparison. *Electr. Power Eng. Technol.* **2026**, *45*, 28–36. (In Chinese)
25. Duan, Y.B.; Xu, Q.W.; Luo, W.; Lan, R.; Li, G.C. Study on XLPE insulation characteristics and temperature field simulation of high-voltage cables with different service years. *Shandong Electr. Power Technol.* **2025**, *52*, 81–88. (In Chinese)

Disclaimer/Publisher's Note: The statements, opinions and data contained in all publications are solely those of the individual author(s) and contributor(s) and not of MDPI and/or the editor(s). MDPI and/or the editor(s) disclaim responsibility for any injury to people or property resulting from any ideas, methods, instructions or products referred to in the content.